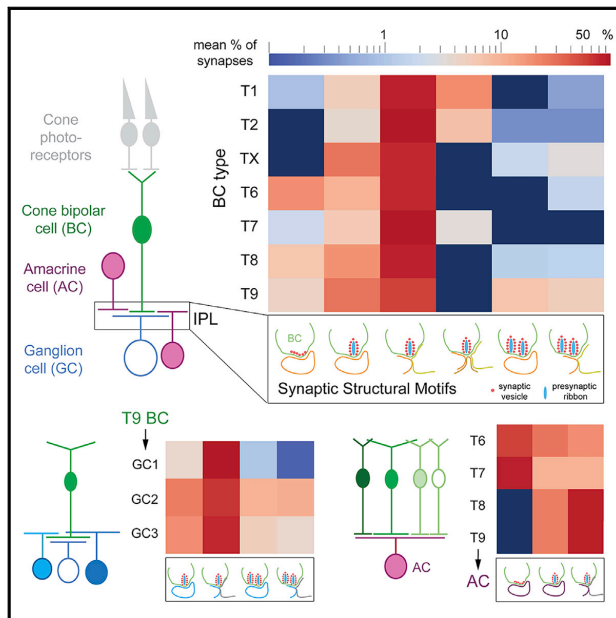


# Cell Reports

## Distinctive synaptic structural motifs link excitatory retinal interneurons to diverse postsynaptic partner types

### Graphical abstract



### Authors

Wan-Qing Yu, Rachael Swanstrom, Crystal L. Sigulinsky, ..., Bryan W. Jones, David M. Berson, Rachel O. Wong

### Correspondence

wongr2@uw.edu

### In brief

Yu et al. find that mouse retinal cone bipolar cells exhibit at least six structurally distinct motifs at their output synapses. The combination of motifs of each bipolar cell type appears stereotypic. Synapses between a bipolar cell type and a postsynaptic partner type are biased toward a subset of motifs.

### Highlights

- Output synapses of cone bipolar cells (CBCs) show six structural motifs
- CBC types differ in their allocation of output synapses to these motifs
- Synaptic monads involving amacrine cells are commonly observed
- CBC synapses with specific partners are biased toward certain motifs



Yu et al., 2023, Cell Reports 42, 112006  
January 31, 2023 © 2023 The Authors.  
<https://doi.org/10.1016/j.celrep.2023.112006>

## Report

# Distinctive synaptic structural motifs link excitatory retinal interneurons to diverse postsynaptic partner types

Wan-Qing Yu,<sup>1</sup> Rachael Swanstrom,<sup>1,5</sup> Crystal L. Sigulinsky,<sup>2,5</sup> Richard M. Ahlquist,<sup>3,5</sup> Sharm Knecht,<sup>1</sup> Bryan W. Jones,<sup>2</sup> David M. Berson,<sup>4</sup> and Rachel O. Wong<sup>1,6,\*</sup>

<sup>1</sup>Department of Biological Structure, University of Washington, Seattle, WA 98195, USA

<sup>2</sup>Department of Ophthalmology, John A. Moran Vision Institute, University of Utah School of Medicine, Salt Lake City, UT 84132, USA

<sup>3</sup>Department of Physiology and Biophysics, University of Washington, Seattle, 98195 WA, USA

<sup>4</sup>Department of Neuroscience, Brown University, Providence, RI 02906, USA

<sup>5</sup>The authors contributed equally

<sup>6</sup>Lead contact

\*Correspondence: [wongr2@uw.edu](mailto:wongr2@uw.edu)

<https://doi.org/10.1016/j.celrep.2023.112006>

## SUMMARY

Neurons make converging and diverging synaptic connections with distinct partner types. Whether synapses involving separate partners demonstrate similar or distinct structural motifs is not yet well understood. We thus used serial electron microscopy in mouse retina to map output synapses of cone bipolar cells (CBCs) and compare their structural arrangements across bipolar types and postsynaptic partners. Three presynaptic configurations emerge—single-ribbon, ribbonless, and multiribbon synapses. Each CBC type exploits these arrangements in a unique combination, a feature also found among rabbit ON CBCs. Though most synapses are dyads, monads and triads are also seen. Altogether, mouse CBCs exhibit at least six motifs, and each CBC type uses these in a stereotypic pattern. Moreover, synapses between CBCs and particular partner types appear biased toward certain motifs. Our observations reveal synaptic strategies that diversify the output within and across CBC types, potentially shaping the distinct functions of retinal microcircuits.

## INTRODUCTION

Synapses are highly diverse in their structural organization, molecular composition, and function. The molecular makeup of pre- and postsynaptic proteins clearly governs the functional properties of synapses,<sup>1–4</sup> but synaptic architecture also plays a major role in shaping neurotransmission. Excitatory synapses often target dendritic spines, which vary in morphology and size across brain regions and even within the arbor of an individual cell.<sup>5–9</sup> Also, a single axonal bouton contacting a dendrite or a dendritic spine may contain one or multiple active zones, the sites of neurotransmitter release.<sup>10–12</sup> These diverse pre- and postsynaptic structural arrangements contribute to the functional heterogeneity of glutamatergic synapses, including differences in synaptic strength.<sup>2,8,13</sup>

Although excitatory synapses are structurally diverse, synapses between specific pairs of neuronal types can be more stereotyped, adopting a specific structural pattern or motif. For example, input synapses to CA3 pyramidal cells contain multiple active zones when they come from dentate granule cells<sup>14,15</sup> but usually just one active zone when they are derived from recurrent CA3-to-CA3 connections.<sup>16</sup> These observations raise the question of whether, in highly converging and diverging circuits, distinct excitatory inputs onto a given postsynaptic cell each

exploit a specific motif. Nor is it known whether an individual axon exploits similar or distinct motifs with each of its several postsynaptic partner types. To gain insight, it is necessary to identify the structural motifs of all the output synapses of a presynaptic cell type and the motifs of multiple input types onto a given postsynaptic cell type. We focused on the vertebrate retina to map these motifs because of its compact circuitry and well-characterized cell types.<sup>17–19</sup>

In the vertebrate retina, cone photoreceptors transmit light-driven signals to cone bipolar cells (CBCs). CBCs are excitatory neurons that synapse onto retinal ganglion cells (GCs) and inhibitory amacrine cells (ACs).<sup>18,20,21</sup> Each of these cell classes comprises many cell types, which are distinguished based on morphology and arbor stratification.<sup>17,22,23</sup> The axonal arbors of CBCs are relatively small, enabling their output synapses to be mapped completely. Classically, BC synapses are synaptic dyads, which contain a single synaptic ribbon localized at a junction with the processes of two postsynaptic partners.<sup>24–26</sup> However, less common arrangements also occur, including BC synapses lacking ribbons or with multiple ribbons<sup>27–33</sup> or with only a single postsynaptic process (synaptic monads).<sup>24,28,34–38</sup> However, it is unknown whether these unconventional CBC synaptic arrangements occur only, or much more commonly, in certain CBC types or if they are more or less similarly distributed



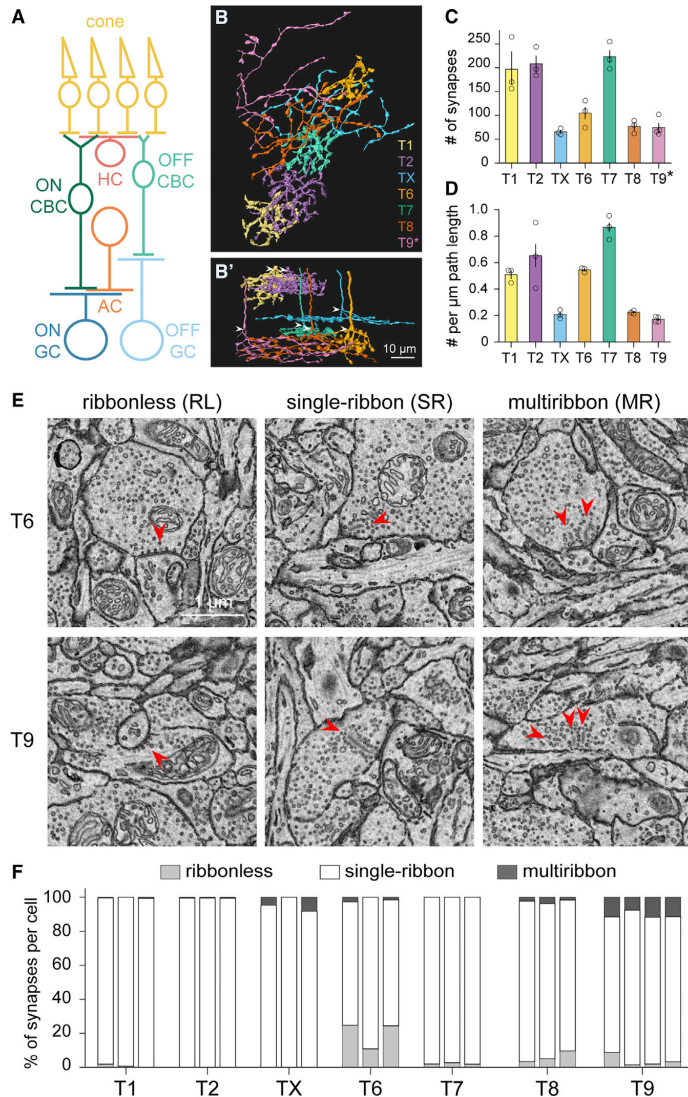


**Figure 1. CBCs exhibit three distinct presynaptic structural arrangements**

(A) Schematic showing ON and OFF cone pathways in the adult mouse retina. Cone, cone photoreceptors; BC, bipolar cells; HC, horizontal cells; AC, amacrine cells; GC, ganglion cells.

(B and B') Axonal terminals of an example of two OFF (T1 and T2) and five ON CBC types (TX, T6, T7, T8, and T9) obtained from serial EM reconstructions. *En face* (B) and side (B') views. \*T9 CBC axonal arbors were only partially reconstructed because their arbor size exceeded the EM volume.

(C and D) Total number of synapses (C) and linear synaptic density (D) of the axonal arbors of the seven types of CBCs analyzed (see STAR Methods). All synapses below the branching point marked by arrowheads in B' were mapped. Numbers above the histograms indicate number of reconstructed cells. Error bars, SEM.

(E) Examples of ribbonless (RL), single-ribbon (SR), and multiribbon (MR) synapses of T6 (top row) and T9 (bottom row) CBCs. Synaptic vesicles at the contact site (RL) or at synaptic ribbons (SR, MR) are indicated by the arrowheads.

(F) The percentage of RL, SR, and MR synapses per cell of each CBC type. See also Figures S1 and S2.

the motifs used by each type of presynaptic CBC. We show that there are in total six structural motifs at mouse CBC synapses and that motif types are non-uniformly distributed among the CBC types. Each CBC type exhibits a stereotypic complement of motif types, and synapses between these CBCs and their postsynaptic partners are biased toward specific motifs.

## RESULTS

### CBCs exhibit three distinct presynaptic arrangements in different proportions across cell types

CBCs are grouped into ON or OFF types according to the polarity of their response to the onset of the light stimulus (Figure 1A). In a novel SBEM volume spanning about 48  $\mu\text{m}$  of the inner plexiform layer (IPL), we reconstructed two types of OFF CBCs (T1 and T2) and five types of ON CBCs (TX, T6, T7, T8, and T9) (Figures 1B and 1B').

These CBCs are easily distinguished by the size and stratification of their axonal terminal arbors (Figure 1B'). T1 CBCs can be distinguished from T2 by their slightly larger and more narrowly stratifying axonal arbors. T6 and T7 CBCs have compact, bushy axonal arbors, whereas T8, T9, and TX CBCs have relatively large, sparse arbors (Figure 1B). T9 axonal arbors could only be partially reconstructed because

across types. We thus used serial block-face scanning electron microscopy (SBEM) to categorize the structural motifs and postsynaptic targets of two types of OFF and five types of ON CBCs in the adult mouse retina.<sup>17,32</sup> We extended the analysis to similar connectomic reconstructions of rabbit ON CBCs based on serial automated transmission electron microscopy (TEM). For each mouse CBC type, we compared the structural motifs used in synaptic contacts onto postsynaptic GCs with those onto ACs. For specific postsynaptic partners, we compared

they extended horizontally outside the volume. Although some *en passant* synapses were also present in axonal shafts as previously reported in mouse retina,<sup>32</sup> we focused on the output synapses of the axonal terminal arbors (Figure 1B') because in some locations, the volume did not extend to the outermost IPL. The total number of synapses differed among mouse CBC types (Figure 1C; see also Tsukamoto and Omori<sup>32</sup>). The linear synaptic density was also type specific, with the two OFF CBC types (T1 and T2) and the smaller ON CBCs (T6 and T7) exhibiting higher synaptic density than the larger ON CBCs (TX, T8, and T9) (Figure 1D).

Three presynaptic structural arrangements were observed in the terminal arbors of the CBC types examined. Most featured a single ribbon (SR), but some had multiple ribbons (multiribbon [MR]). Others lacked any ribbon at all (ribbonless [RL]), instead consisting only of docked synaptic vesicles lining the presynaptic membrane at the synaptic cleft (Figure 1E). Locations of these three presynaptic arrangements did not appear to be restricted to specific parts or stratification depths of the axonal arbors (Figure S1). As expected from past work, the majority of the CBC output synapses were SR synapses (Figure 1F). However, the majority of CBC types we examined also made RL synapses; only T2 and TX CBCs lacked them. RL synapses were significantly more common in T6 BCs than in the other CBC types (Figure 1F; Kruskal-Wallis H test:  $p = 0.004$ , post-hoc Wilcoxon rank-sum test:  $p < 0.05$ ). MR synapses, in contrast, were found more frequently on T9 than other types of CBC arbors (Figure 1F; Kruskal-Wallis H test:  $p = 0.022$ , post-hoc Wilcoxon rank-sum test:  $p < 0.05$ ). The proportions of these presynaptic arrangements were consistent within the same CBC type (chi-squared test:  $p > 0.05$  for each individual BC type) but were distinct across CBC types (chi-squared test across five BC types:  $p < 0.001$ ).

The consistent proportions of "unconventional" MR and RL synapses among members of each individual CBC type suggest that both these synapse types are unlikely to be vestiges of development. To determine whether this pattern is a general feature of mammalian retinas, we quantified synapses in ON CBCs in another species, exploiting an existing serial-section transmission electron microscopic volume of the rabbit retina (retinal connectome 1 [RC1]<sup>38</sup>). The rabbit retina has been shown to contain seven types of ON CBCs, CBb3, CBb3n, CBb4, CBb4w, CBb5, CBb6, and CBbwf, each exhibiting stereotyped morphology (Figures S2A and S2A') and connectivity.<sup>33</sup> As in mice, and consistent with previous whole axon synapse counts in RC1, the total number of output synapses in the axon terminals varied across the different rabbit ON CBC types (Figure S2B; see also Sigulinsky et al.<sup>33</sup> and Lauritzen et al.<sup>40,41</sup>). Re-examination of these output synapses confirmed that all three types of presynaptic structural arrangements were observed in rabbit ON CBC axonal arbors (Figure S2C; see also Sigulinsky et al.<sup>33</sup>), with SR synapses by far the most common for all rabbit CBC types (Figure S2D; chi-squared test:  $p > 0.05$  for each individual CBC type;  $p < 0.001$  across 7 CBC types). As in mice, proportions of the three presynaptic arrangements differed among rabbit ON CBC types. Together, our observations show that CBCs in both mice and rabbits make unconventional RL and MR synapses as well as classical SR synapses in proportions that are stereotyped for each CBC type.

### CBCs utilize diverse synaptic structural arrangements for excitatory transmission

We examined the number of postsynaptic partners at each synaptic output site of the mouse CBCs we mapped. Synaptic dyads, with two postsynaptic partners, were the predominant postsynaptic structural arrangement (range 59.8%–89.1% across CBC types examined). However, synaptic monads (with a single postsynaptic partner) were also common (4.1%–40.2%), while triads (three postsynaptic partners) were less common (0%–19.6%). Monads, dyads, and triads were unevenly distributed among the three presynaptic arrangements. Synaptic monads occurred for all three, but triads were found only at SR synapses, and dyads were always associated with ribbons and never with RL synapses (Table S1). Together, these rules define six synaptic structural motifs, each with a unique pre- and postsynaptic arrangement: RL and SR monads, SR dyads and triads, and MR monads and dyads (Figure 2A). SR synapses were predominantly dyads (Figure 2B, left), but all CBC types examined also make SR monads, albeit in different proportions (Kruskal-Wallis H test:  $p = 0.003$ ). SR monads were most common for TX and T9 CBCs. Synaptic triads were observed in both OFF CBCs (T1 and T2) and in T7 ON CBCs, and they are most common in T1 CBCs. MR synapses can be either monads or dyads (Figure 2B, right). However, except for T6 CBCs, there does not seem to be any preference for monads or dyads for the other CBC types that have MR synapses (Figure 2B, right; chi-squared test:  $p = 0.03$  for T6,  $p > 0.05$  for other CBC types).

The distribution of these six motifs among CBC types is summarized in Figure 2C. It shows that the classical SR dyad is the most common motif among all the types examined, with SR monads and RL monads the next most common. It also highlights how each CBC type exploits the various motifs in a unique proportion.

### Synapses between CBCs and their postsynaptic partners are biased toward specific structural motifs

To examine how CBCs utilize these distinct synaptic arrangements, we determined the postsynaptic partner class arrangements of the three most common motifs. At SR dyads, the paired postsynaptic partners engaged by the CBC can comprise two ACs, two GCs, or one of each.<sup>42–46</sup> In primate and cat, GC/AC pairs predominate at IPL dyads.<sup>42–44</sup> Our analysis indicated that this was largely true overall among mouse CBCs and confirmed it individually for types T2, T6, T8, and T9 CBCs (Figure 3A). However, in T1, TX, and T7 cells, GC/AC dyads were outnumbered by AC/AC dyads. In general, GC/GC postsynaptic pairs were much less common than AC/AC pairs (Figure 3A). In T2 CBC arbors, we observed non-traditional synaptic dyads in which one postsynaptic partner was another CBC. The other synaptic partner in this dyad arrangement was invariably an AC (Figure S3A). Postsynaptic AC partners at ribbon dyads can make a reciprocal inhibitory synapse onto CBC axon terminals (Figure S3B) and/or feedforward inhibition to the other postsynaptic partner (Figure S3C). The fraction of ribbon dyads with at least one reciprocal inhibitory synapse varied across CBC types (Figure S3D; Kruskal-Wallis H test:  $p = 0.005$ ). Reciprocal inhibitory synapses were most frequently observed among T1 CBCs

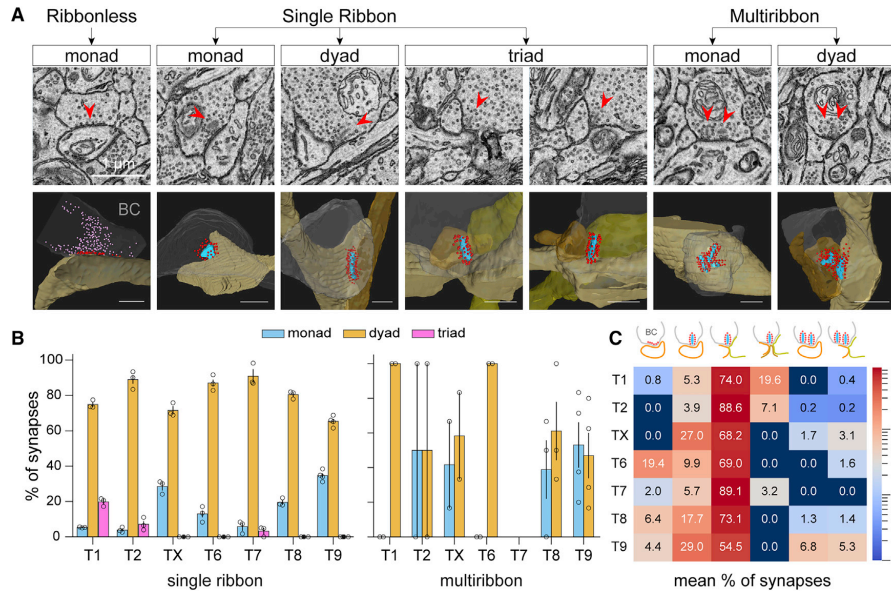


**Figure 2. CBCs exhibit diverse synaptic structural motifs at their output sites**

(A) Example EM images (top row) and 3D reconstructions (bottom row) of each synaptic structural motif observed among CBC output synapses. Clustered presynaptic vesicles at synaptic junctions or synaptic ribbons are indicated by arrows in the EM images. In the 3D reconstructions, red dots indicate vesicles docked at the active zone (RL monad) or surrounding the presynaptic ribbons (cyan) in the CBC (gray) terminals; postsynaptic neurons are in shades of brown. Vesicles not docked at the active zone in the RL monad are colored pink.

(B) Proportion of SR (left plot) and MR (right plot) synapses that were monads, dyads, or triads across CBC types. Each data point represents a CBC. Error bars, SEM.

(C) Heatmap illustrating the mean percentage of all synapses formed by each CBC type belonging to each motif (schematized at the top). Number of cells and SEM for each CBC type are provided in (B). See also [Table S1](#).

(post-hoc Wilcoxon rank-sum test:  $p < 0.05$ ). The fraction of ribbon dyads demonstrating feedforward inhibition also varied across CBC types (Figure S3E; Kruskal-Wallis H test:  $p = 0.007$ ).

We identified the sole postsynaptic partner class of each monad synapse and compared the pattern across CBC types (Figure 3B). Monad synapses of the SR type targeted more ACs than GCs (chi-squared test:  $p < 0.001$ ) for most CBC types analyzed, including T1, TX, T6, T7, and T8. However, T9 CBCs favored GCs over ACs at such SR monads (chi-squared test:  $p < 0.001$ ), while T2 CBCs had no clear preference for either cell class (chi-squared test:  $p = 0.8$ ). The RL monads of T6, T7, and T8 CBCs showed the same preference for ACs as the postsynaptic partners (chi-squared test:  $p < 0.001$ ; Figure 3B) as seen among SR monads. In contrast, T1 and T9 CBCs exhibited no class preference at these synapses (chi-squared test:  $p > 0.1$ ). Figure 3C summarizes the proportion of synapses of each CBC type bearing the common structural motifs. Together, these findings suggest that structural motifs are employed in distinct patterns by specific bipolar types and their postsynaptic partner classes.

Each CBC contacts many postsynaptic cell types. For example, T2 CBCs made ribbon synapses onto at least 14 (10

RGC and 4 narrow-field AC types). Similarly, T6 CBCs contacted at least 12 (8 RGC and 4 narrow-field AC types) cell types through ribbon synapses (Figure S4). To determine whether a CBC type uses distinct synaptic arrangements at contacts with different postsynaptic partner types, we mapped the output connectivity of a single CBC type (T9) with several GC partner types in an existing, larger volume of adult mouse IPLs<sup>47</sup> (Figure 4A). We focused on these CBCs because they rely more heavily on non-classical output synapses, differing from the SR dyad arrangement. Prior reconstructions in this volume showed that T9 CBCs contact M5 GCs<sup>48</sup> as well as a pair of cell types that resemble M2 GCs.<sup>49</sup> These are divisible into two types termed M2(8) and M2(9) to reflect their differential weighting of inputs from T8 and T9 CBCs. We determined the motifs of all T9 synapses onto three examples of each GC type. We found that the T9 CBCs made SR monads and dyads and MR monads and dyads onto these GC types (Figure 4B). MR synapses and monad synapses were less common, and both preferentially targeted M2(9) and M5 GCs over M2(8) cells (MR: Figure 4C left, chi-squared test:  $p < 0.001$ ; monads: Figure 4C, middle, chi-squared test:  $p < 0.001$ ). The allocation of T9 synapses across the four structural motifs was statistically different for synapses onto M2(8)

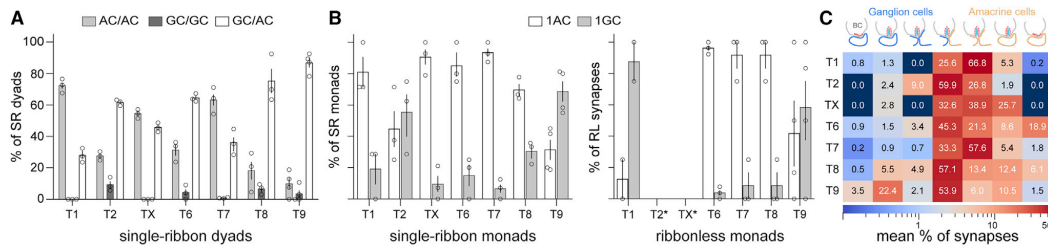


**Figure 3. Monad synapses are commonly formed between CBCs and ACs**  
(A) Proportions of single-ribbon dyads involving two amacrine cells (AC/AC), two ganglion cells (GC/GC), or one amacrine and one ganglion cell (GC/AC).  
(B) Proportions of single-ribbon monads (left) or ribbonless monads (right) formed between a CBC and a ganglion cell (1GC) or an amacrine cell (1AC).  
(C) Heatmap illustrating the mean percentage of each structural motif schematized above involving the different types of CBCs and GC or AC partners. Number of cells and SEM for each BC type are provided in (A) and (B). See also Figure S3 and Table S1.

cells compared with those onto M2(9) and M5 GCs (Figure 4C, right; chi-squared test:  $p < 0.05$ ).

We also compared the motifs of the different CBC types providing converging input onto a common postsynaptic target, a polyaxonal AC (Figure 4D). Consistent with previous studies,<sup>50–52</sup> synaptic inputs from CBCs were located exclusively onto the dendritic processes of this polyaxonal AC within the limit of the EM volume. Among four CBC input types identified, T6 and T7 were the major input types, and T8 and T9 provided sparser input. Three distinct motifs were observed: RL and SR monads and SR dyads (Figures 4E and 4F). RL monads made up more than half of the synapses between T6 and T7 CBCs with this AC. However, they were absent from T8 and T9 synapses onto this cell (Figure 4G), though these bipolar types do make such synapses with other AC types (Figures 3B and 3C). Moreover, T8 and T9 CBCs preferentially made SR dyads with this polyaxonal AC. Together, these observations suggest that while synapses between ON CBCs and their targets show a large variety of structural motifs overall, these motifs may be differentially engaged between a CBC type and a postsynaptic partner type.

## DISCUSSION

### CBC synapses exhibit diverse motifs with stereotypic structural combinations across cell types

It is well established that in the vertebrate retina, both rod and cone BCs form ribbon synapses, especially ribbon dyads, with their postsynaptic partners.<sup>24,25</sup> We confirmed this here in mouse retina for the output synapses of all seven CBC types we studied. However, we also identified five other output motifs for these CBCs. This differentiates cone BCs from rod BCs, which employ SR dyads almost exclusively.<sup>26,53</sup> These five CBC output motifs include SR or RL monads, SR triads, or MR monads or dyads. SR monads and triads have been reported previously in the IPL of the retina of several species including salamander, rabbit, and primate.<sup>27,35,37,54</sup> MR synapses are common in both rod BCs and CBCs that have reduced glutamate release<sup>55</sup> due to transgene expression of tetanus toxin,<sup>56</sup> but they have thus far been found in wild-type retina within the

axon shaft of ON CBCs in mice and rabbits and only in synaptic monads.<sup>49,57</sup> Our data show that MR synapses are not uncommon in the axonal terminals of CBCs in wild-type mice and rabbits, appearing, at least in mice, as dyads in addition to monads. RL synapses, some apparently forming monad synapses, have been noted in the IPL of salamander,<sup>27</sup> rabbit,<sup>30,33,58</sup> human and non-human primate,<sup>28,29</sup> and goldfish retinas.<sup>59</sup> Our analysis suggests that RL synapses in mouse CBCs are exclusively monads. While not all of these unconventional CBC motifs are novel, to the best of our knowledge, our current analysis is the first to quantify their relative abundance among specific CBC types.

These five unconventional motifs can be found at both OFF and ON CBC axonal terminals. Further, each CBC type exploited at least three of the five unconventional motifs. Thus, each CBC type exhibits a diversity of motifs, yet no type uses every motif. The allocation of output synapses among the possible motifs is stereotyped for each CBC type. For example, SR monads, rarely observed previously,<sup>27,28,34,35,38</sup> were surprisingly common and type specific, comprising 4%–29% of output synapses among the CBC types we studied. SR triads were more frequently used by OFF CBCs than by ON CBCs, at least among the subset of types analyzed here. The stereotypic compositions of motifs of each of the mouse CBC types studied suggest that this is a functionally significant aspect of CBC connectivity.

Given that each CBC type uses a stereotypic combination of output motifs, we wondered whether connections with distinct postsynaptic partner types involve a specific motif or subset of motifs. We found that CBC-GC synapses (except those of T9) are mostly SR dyads, whereas CBC-AC synapses comprise of a mixture of motifs (SR dyads, SR monads, and RL monads). In addition, a presynaptic CBC type (T9) can preferentially make unconventional synapses such as MR synapses or ribbon monads with some of its postsynaptic partner types and not others. Furthermore, the unconventional motifs (i.e., RL monads) could be the dominant motif between some CBC types and a given postsynaptic partner. Different motifs at connections involving a given presynaptic cell type and distinct postsynaptic partners have been shown for layer III long-range projection neurons of the entorhinal cortex. These cortical neurons

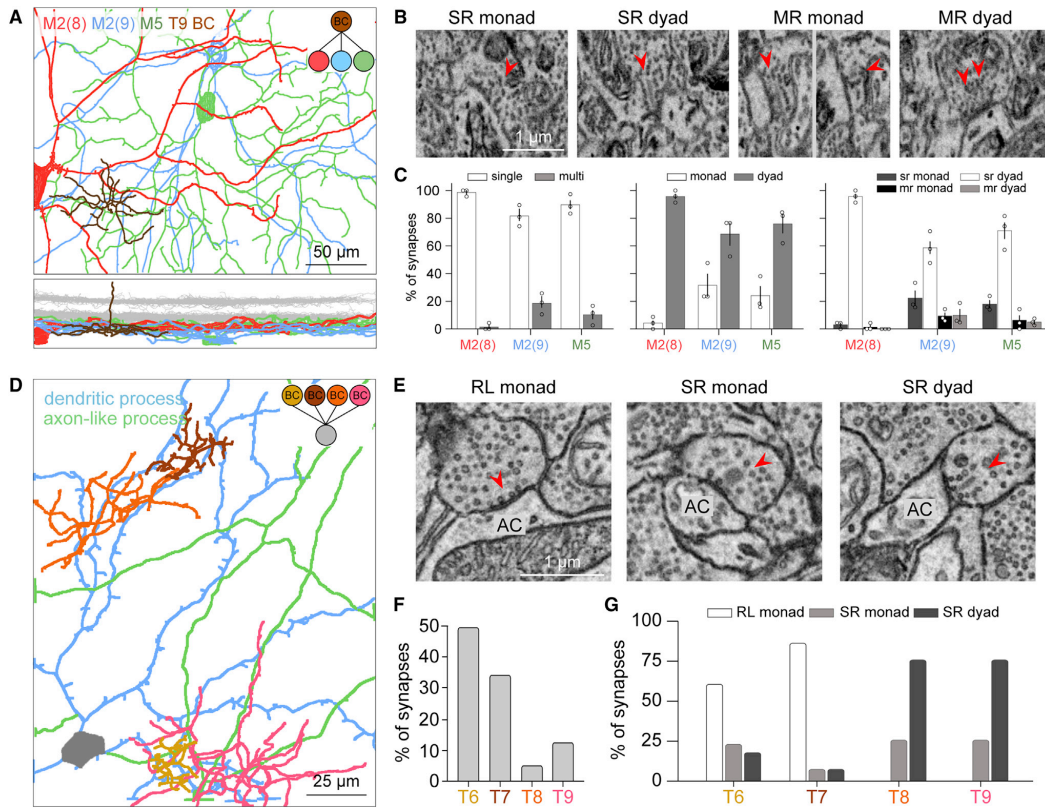


**Figure 4. CBCs demonstrate a bias in their structural motifs at synapses formed with specific postsynaptic cell types**

(A–C) T9 CBCs preferentially make MR synapses or SR monads with some GC types.

(A) Dendritic skeletons of M2(8), M2(9), and M5 GCs and an example axonal terminal of a T9 CBC contacting all three GCs. Top: *en face* view; bottom: side view showing dendritic and axonal stratifications of the cells in the inner plexiform layer relative to the processes of cholinergic ACs.

(B) EM images of different motifs (SR and MR) at synapses formed between T9 CBCs and an M2(9) GC. Arrows indicate ribbons.

(C) Proportions of synapses that were SR or MR (left), and synapses that were monads or dyads (middle) formed with each GC type analyzed. Right: proportions of four motifs of synapses between T9 CBCs and the three GCs. Each data point represents a GC cell. Error bars, SEM.

(D–G) A polyaxonal AC preferentially forms RL synapses with ON CBCs.

(D) Skeleton of the polyaxonal AC showing its dendritic (blue) and axonal (green) processes.

(E) EM images providing an example of an RL monad, an SR monad, and an SR dyad at synapses (arrowheads) along the AC dendrites.

(F) Percentage of synapses of four types of ON CBCs (T6, T7, T8, and T9) contacting this AC.

(G) Proportions of reconstructed synapses with different motifs between the various CBC types and the polyaxonal AC.

See also Figure S4.

preferentially form spatially clustered synapses onto CA1 pyramidal cells in the hippocampus compared with their other targets in the basolateral amygdala.<sup>60</sup> Unlike layer III cortical neurons, however, the retinal CBCs have short-range axons that contact different postsynaptic cell types within a local area. Our findings would thus suggest that a biased selection of synaptic structural motifs is dependent on postsynaptic partner types regardless of their location.

Conversely, postsynaptic neurons often receive converging inputs from different presynaptic cell types. The CA1 pyramidal

neurons receive synaptic input not only from the entorhinal cortex but also from neurons of the midline thalamus.<sup>61–63</sup> However, the thalamic synapses onto the CA1 neurons rarely form clusters, in contrast to the entorhinal cortical synapses.<sup>60</sup> Likewise, we found that the converging synapses of four distinct CBC types onto a polyaxonal AC exhibit biases toward different motifs. In addition, our data suggest that the CBC types that provide the major synaptic drive onto a given postsynaptic cell “prefer” a particular motif/set of motifs that are distinct from that of the minor inputs. Our current and past findings suggest that diversity



in synaptic transmission across excitatory input types may be attained not only by distinct molecular composition at their synapses (e.g., receptor composition) but also by differences in synaptic architecture.

#### Functional implications of diverse synaptic structural motifs of BC circuitry

Various synaptic architectures contribute to functional diversity at glutamatergic synapses.<sup>4</sup> For example, synapses with multiple transmitter release sites often evoke larger postsynaptic currents than synapses with only a single release site.<sup>5</sup> Hence, CBC synapses with distinct presynaptic structural arrangements could enable transmission with different amplitude and/or kinetics at CBC synapses. Indeed, previous work suggests that RL and ribbon synapses on BC axon terminals show distinct temporal kinetics in neurotransmitter release. At ribbon synapses, docked vesicles at the base of the ribbon support a rapid initial transient of excitation, and the ribbon also supports the steady-state transmitter release.<sup>64</sup> In contrast, RL synapses exhibit delayed and unsynchronized transmitter release.<sup>59,65–67</sup> Glutamate imaging of mouse ON CBCs showed that transmitter release at MR *en passant* synapses at axonal shafts is similar to that at SR synapses at the axonal terminals, though apparently weaker.<sup>49</sup> This may be due to the relatively smaller size of individual ribbons present in MR synapses.<sup>57</sup> We also observed MR synapses formed by the axonal terminals of several mouse CBC types, but the sizes of these ribbons appeared to be comparable to those found at SR synapses. Thus, individual MR synapses at the CBC axonal terminals might facilitate a larger synaptic drive compared with the SR synapses.

CBCs exhibited biases in their synaptic arrangements with specific postsynaptic partner types. For example, T9 CBCs preferentially make MR synapses with M5 intrinsically photosensitive RGCs (ipRGCs) and with the M2(9) GC type, which may or may not correspond to M2 ipRGCs.<sup>49</sup> ON CBC axonal shafts are known to make exclusively MR synapses onto M1 ipRGCs. Thus, it appears that synapses between at least some ON CBC types and ipRGCs “favor” an MR synaptic arrangement. What is the advantage of having an MR synapse between CBCs and ipRGCs? The dendritic arbor of M1 ipRGCs is sparsely branching, which results in a low contact density with the axon shafts of the ON CBCs. Similarly, T9 CBCs have large and sparsely branching axonal arbors with low output synapse density. MR synapses may compensate for the sparser synaptic connections between certain ON CBCs and ipRGCs, possibly facilitating a robust synaptic drive that could underlie the sustained ON response of ipRGCs.<sup>68,69</sup>

Our observations also suggest the engagement of two other synaptic arrangements that would facilitate an undiminished drive from CBCs with sparse connectivity with the ipRGCs. We found that monads involving T9 CBCs were largely with the two ipRGC types. GC/GC dyads were also more frequently observed for T6, T8, and T9 ON CBCs, the major CBC input types of ipRGCs.<sup>49</sup> GC/GC dyads were shown previously between ON BCs and a pair of M5 ipRGCs.<sup>48</sup> The absence of AC postsynaptic partners at GC monads and GC/GC dyads may buffer the CBCs feeding ipRGCs from local feedback inhibition present at other dyad synapses, therefore enhancing the net postsynaptic drive.

Future work is needed to establish the structure-function relationships of the CBC synapses with different structural arrangements. Indeed, further diversity across CBC synapses may be uncovered by future studies that link molecular composition and other synapse features to each of the structural motifs we demonstrate here.

#### Limitations of the study

The ultrastructural reconstructions and analyses were carried out manually, and thus we limited our analysis to 3 to 4 cells of a subset of ON and OFF CBC types in one volume each from a mouse and a rabbit retina. Future analysis in other samples at different retinal locations or of different sex would be valuable. The thickness of the section for the mouse EM volume was 50 nm. It posed challenges in identifying ribbons that oriented obliquely. However, >90% of the synapses could be tracked in more than one section. Overall, it is unlikely that we missed a significant number of synapses in our analysis because the total number of ribbon synapses we obtained is either comparable or more than that previously found for the same BC types<sup>32,70,71</sup> Because of the size limitation of our mouse EM volume, not every process classified as a GC process could be traced back to the cell body and axon. Hence, it is possible that some of the partners identified as GCs may be the dendritic arbors of polyaxonal ACs whose somata lie outside the volume.

#### STAR★METHODS

Detailed methods are provided in the online version of this paper and include the following:

- KEY RESOURCES TABLE
- RESOURCE AVAILABILITY
  - Lead contact
  - Materials availability
  - Data and code availability
- EXPERIMENTAL MODEL AND SUBJECT DETAILS
- METHOD DETAILS
  - Tissue preparation and serial-block face electron microscopy
  - Volume reconstruction and image analysis
- QUANTIFICATION AND STATISTICAL ANALYSIS

#### SUPPLEMENTAL INFORMATION

Supplemental information can be found online at <https://doi.org/10.1016/j.celrep.2023.112006>.

#### ACKNOWLEDGMENTS

We thank Rebecca L. Pfeiffer, Christopher N. Rapp, Daniel P. Emrich, Hope Morrison, J. Scott Lauritzen, John Hoang, Alex Sessions, Nicholas McCarthy, and Andrea Bordt for cell tracing in the RC1 dataset. We also thank Chi-Chou Huang, Hideki Sasaki, Luciano A.G. Lucas, and James S.J. Lee from Leica Aivia for providing tools to stitch and register the mouse EM volume. The scanning electron microscopy used in this study was supported by NEI center core grant for vision research EY01730 to Maureen Neitz. This work was supported by National Institutes of Health grants R01 EY10699 and SBIR MH121167 to R.O.W., R01 EY12793 to D.M.B., R01 EY015128 and R01 EY028927 to B.W.J., P30 EY014800 to Core, and T32 EY024234 to C.L.S.; an NSF NN2



2014862 to B.W.J.; and Research to Prevent Blindness (New York) Unrestricted Grant to the Department of Ophthalmology & Visual Sciences, University of Utah. Funding for the JEOL JEM-1400 was generously provided by the late Martha Ann Healy, a friend of the Moran Eye Center.

#### AUTHOR CONTRIBUTIONS

Conceptualization, W.-Q.Y. and R.O.W.; methodology and investigation, W.-Q.Y, R.S., R.M.A., C.L.S., S.K., and D.M.B.; formal analysis, W.-Q.Y. and C.L.S.; writing – original draft, W.-Q.Y., C.L.S., and R.O.W.; writing – review & editing, W.-Q.Y., C.L.S., B.W.J., D.M.B., and R.O.W.

#### DECLARATION OF INTERESTS

The authors declare no competing interests.

#### INCLUSION AND DIVERSITY

We support inclusive, diverse, and equitable conduct of research.

Received: April 26, 2022

Revised: November 9, 2022

Accepted: January 3, 2023

#### REFERENCES

- Craig, A.M., and Boudin, H. (2001). Molecular heterogeneity of central synapses: afferent and target regulation. *Nat. Neurosci.* 4, 569–578. <https://doi.org/10.1038/88388>.
- Atwood, H.L., and Karunanithi, S. (2002). Diversification of synaptic strength: presynaptic elements. *Nat. Rev. Neurosci.* 3, 497–516. <https://doi.org/10.1038/nrn876>.
- O'Rourke, N.A., Weiler, N.C., Micheva, K.D., and Smith, S.J. (2012). Deep molecular diversity of mammalian synapses: why it matters and how to measure it. *Nat. Rev. Neurosci.* 13, 365–379. <https://doi.org/10.1038/nrn3170>.
- Wichmann, C., and Kuner, T. (2022). Heterogeneity of glutamatergic synapses: cellular mechanisms and network consequences. *Physiol. Rev.* 102, 269–318. <https://doi.org/10.1152/physrev.00039.2020>.
- Wilson, C.J., Groves, P.M., Kitai, S.T., and Linder, J.C. (1983). Three-dimensional structure of dendritic spines in the rat neostriatum. *J. Neurosci.* 3, 383–388.
- Harris, K.M., and Kater, S.B. (1994). Dendritic spines: cellular specializations imparting both stability and flexibility to synaptic function. *Annu. Rev. Neurosci.* 17, 341–371. <https://doi.org/10.1146/annurev.ne.17.030194.002013>.
- Arellano, J.I., Benavides-Piccione, R., Defelipe, J., and Yuste, R. (2007). Ultrastructure of dendritic spines: correlation between synaptic and spine morphologies. *Front. Neurosci.* 1, 131–143. <https://doi.org/10.3389/neuro.01.1.1.010.2007>.
- Parajuli, L.K., Urakubo, H., Takahashi-Nakazato, A., Ogelman, R., Iwasaki, H., Koike, M., Kwon, H.B., Ishii, S., Oh, W.C., Fukazawa, Y., and Okabe, S. (2020). Geometry and the organizational principle of spine synapses along a dendrite. *eNeuro* 7, ENEURO.0248.20.2020. <https://doi.org/10.1523/ENEURO.0248-20.2020>.
- Parajuli, L.K., and Koike, M. (2021). Three-Dimensional structure of dendritic spines revealed by volume electron microscopy techniques. *Front. Neuroanat.* 15, 627368. <https://doi.org/10.3389/fnana.2021.627368>.
- Blackstad, T.W., and Kjaerheim, A. (1961). Special axo-dendritic synapses in the hippocampal cortex: electron and light microscopic studies on the layer of mossy fibers. *J. Comp. Neurol.* 117, 133–159. <https://doi.org/10.1002/cne.901170202>.
- Hoogland, P.V., Wouterlood, F.G., Welker, E., and Van der Loos, H. (1991). Ultrastructure of giant and small thalamic terminals of cortical origin: a study of the projections from the barrel cortex in mice using Phaseolus vulgaris leuco-agglutinin (PHA-L). *Exp. Brain Res.* 87, 159–172. <https://doi.org/10.1007/BF00228517>.
- Chicurel, M.E., and Harris, K.M. (1992). Three-dimensional analysis of the structure and composition of CA3 branched dendritic spines and their synaptic relationships with mossy fiber boutons in the rat hippocampus. *J. Comp. Neurol.* 325, 169–182. <https://doi.org/10.1002/cne.903250204>.
- Bellot, A., Guivernau, B., Tajés, M., Bosch-Morató, M., Valls-Comamala, V., and Muñoz, F.J. (2014). The structure and function of actin cytoskeleton in mature glutamatergic dendritic spines. *Brain Res.* 1573, 1–16. <https://doi.org/10.1016/j.brainres.2014.05.024>.
- Claiborne, B.J., Amaral, D.G., and Cowan, W.M. (1986). A light and electron microscopic analysis of the mossy fibers of the rat dentate gyrus. *J. Comp. Neurol.* 246, 435–458. <https://doi.org/10.1002/cne.902460403>.
- Henze, D.A., Urban, N.N., and Barrionuevo, G. (2000). The multifarious hippocampal mossy fiber pathway: a review. *Neuroscience* 98, 407–427. [https://doi.org/10.1016/s0306-4522\(00\)00146-9](https://doi.org/10.1016/s0306-4522(00)00146-9).
- Le Duigou, C., Simonnet, J., Teleńczuk, M.T., Fricker, D., and Miles, R. (2014). Recurrent synapses and circuits in the CA3 region of the hippocampus: an associative network. *Front. Cell. Neurosci.* 7, 262. <https://doi.org/10.3389/fncel.2013.00262>.
- Helmstaedter, M., Briggman, K.L., Turaga, S.C., Jain, V., Seung, H.S., and Denk, W. (2013). Connectomic reconstruction of the inner plexiform layer in the mouse retina. *Nature* 500, 168–174. <https://doi.org/10.1038/nature12346>.
- Masland, R.H. (2001). The fundamental plan of the retina. *Nat. Neurosci.* 4, 877–886. <https://doi.org/10.1038/nn0901-877>.
- Wässle, H., and Boycott, B.B. (1991). Functional architecture of the mammalian retina. *Physiol. Rev.* 71, 447–480. <https://doi.org/10.1152/physrev.1991.71.2.447>.
- Demb, J.B., and Singer, J.H. (2015). Functional circuitry of the retina. *Annu. Rev. Vis. Sci.* 1, 263–289. <https://doi.org/10.1146/annurev-vision-082114-035334>.
- Diamond, J.S. (2017). Inhibitory interneurons in the retina: types, circuitry, and function. *Annu. Rev. Vis. Sci.* 3, 1–24. <https://doi.org/10.1146/annurev-vision-102016-061345>.
- Euler, T., Haverkamp, S., Schubert, T., and Baden, T. (2014). Retinal bipolar cells: elementary building blocks of vision. *Nat. Rev. Neurosci.* 15, 507–519.
- Bae, J.A., Mu, S., Kim, J.S., Turner, N.L., Tartavull, I., Kernitz, N., Jordan, C.S., Norton, A.D., Silversmith, W.M., Prentki, R., et al. (2018). Digital museum of retinal ganglion cells with dense anatomy and physiology. *Cell* 173, 1293–1306.e19. <https://doi.org/10.1016/j.cell.2018.04.040>.
- Dubin, M.W. (1970). The inner plexiform layer of the vertebrate retina: a quantitative and comparative electron microscopic analysis. *J. Comp. Neurol.* 140, 479–505. <https://doi.org/10.1002/cne.901400406>.
- Dowling, J.E., and Werblin, F.S. (1971). Synaptic organization of the vertebrate retina. *Vis. Res. Suppl* 3, 1–15. [https://doi.org/10.1016/0042-6989\(71\)90026-5](https://doi.org/10.1016/0042-6989(71)90026-5).
- Kolb, H., and Famiglietti, E.V. (1974). Rod and cone pathways in the inner plexiform layer of cat retina. *Science* 186, 47–49. <https://doi.org/10.1126/science.186.4158.47>.
- Wong-Riley, M.T. (1974). Synaptic organization of the inner plexiform layer in the retina of the tiger salamander. *J. Neurocytol.* 3, 1–33.
- Kolb, H., and Dekorver, L. (1991). Midget ganglion cells of the parafovea of the human retina: a study by electron microscopy and serial section reconstructions. *J. Comp. Neurol.* 303, 617–636. <https://doi.org/10.1002/cne.903030408>.
- Grünert, U., Haverkamp, S., Fletcher, E.L., and Wässle, H. (2002). Synaptic distribution of ionotropic glutamate receptors in the inner plexiform layer of the primate retina. *J. Comp. Neurol.* 447, 138–151. <https://doi.org/10.1002/cne.10220>.
- Famiglietti, E.V. (2005). Synaptic organization of complex ganglion cells in rabbit retina: type and arrangement of inputs to directionally selective and

- local-edge-detector cells. *J. Comp. Neurol.* 484, 357–391. <https://doi.org/10.1002/cne.20433>.
31. Bleckert, A., Parker, E.D., Kang, Y., Pancaroglu, R., Soto, F., Lewis, R., Craig, A.M., and Wong, R.O.L. (2013). Spatial relationships between GABAergic and glutamatergic synapses on the dendrites of distinct types of mouse retinal ganglion cells across development. *PLoS One* 8, e69612. <https://doi.org/10.1371/journal.pone.0069612>.
  32. Tsukamoto, Y., and Omi, N. (2017). Classification of mouse retinal bipolar cells: type-specific connectivity with special reference to rod-driven All amacrine pathways. *Front. Neuroanat.* 11, 92. <https://doi.org/10.3389/fnana.2017.00092>.
  33. Sigulinsky, C.L., Anderson, J.R., Kerzner, E., Rapp, C.N., Pfeiffer, R.L., Rodman, T.M., Emrich, D.P., Rapp, K.D., Nelson, N.T., Lauritzen, J.S., et al. (2020). Network architecture of gap junctional coupling among parallel processing channels in the mammalian retina. *J. Neurosci.* 40, 4483–4511. <https://doi.org/10.1523/JNEUROSCI.1810-19.2020>.
  34. Hokoç, J.N., and Mariani, A.P. (1988). Synapses from bipolar cells onto dopaminergic amacrine cells in cat and rabbit retinas. *Brain Res.* 467, 17–26. [https://doi.org/10.1016/0006-8993\(88\)90721-4](https://doi.org/10.1016/0006-8993(88)90721-4).
  35. Calkins, D.J., Tsukamoto, Y., and Sterling, P. (1998). Microcircuitry and mosaic of a blue-yellow ganglion cell in the primate retina. *J. Neurosci.* 18, 3373–3385.
  36. Ghosh, K.K., and Grünert, U. (1999). Synaptic input to small bistratified (blue-ON) ganglion cells in the retina of a new world monkey, the marmoset *Callithrix jacchus*. *J. Comp. Neurol.* 413, 417–428. [https://doi.org/10.1002/\(sici\)1096-9861\(19991025\)413:3<417::aid-cne5>3.0.co;2-h](https://doi.org/10.1002/(sici)1096-9861(19991025)413:3<417::aid-cne5>3.0.co;2-h).
  37. Marc, R.E., and Liu, W. (2000). Fundamental GABAergic amacrine cell circuitries in the retina: nested feedback, concatenated inhibition, and axosomatic synapses. *J. Comp. Neurol.* 425, 560–582. [https://doi.org/10.1002/1096-9861\(20001002\)425:4<560::aid-cne7>3.0.co;2-d](https://doi.org/10.1002/1096-9861(20001002)425:4<560::aid-cne7>3.0.co;2-d).
  38. Bordt, A.S., Perez, D., Tseng, L., Liu, W.S., Neitz, J., Patterson, S.S., Famiglietti, E.V., and Marshak, D.W. (2019). Synaptic inputs from identified bipolar and amacrine cells to a sparsely branched ganglion cell in rabbit retina. *Vis. Neurosci.* 36, E004. <https://doi.org/10.1017/S0952523819000014>.
  39. Anderson, J.R., Jones, B.W., Watt, C.B., Shaw, M.V., Yang, J.H., Demill, D., Lauritzen, J.S., Lin, Y., Rapp, K.D., Mastronarde, D., et al. (2011). Exploring the retinal connectome. *Mol. Vis.* 17, 355–379.
  40. Lauritzen, J.S., Anderson, J.R., Jones, B.W., Watt, C.B., Mohammed, S., Hoang, J.V., and Marc, R.E. (2013). ON cone bipolar cell axonal synapses in the OFF inner plexiform layer of the rabbit retina. *J. Comp. Neurol.* 521, 977–1000. <https://doi.org/10.1002/cne.23244>.
  41. Lauritzen, J.S., Sigulinsky, C.L., Anderson, J.R., Kalloniatis, M., Nelson, N.T., Emrich, D.P., Rapp, C., McCarthy, N., Kerzner, E., Meyer, M., et al. (2019). Rod-cone crossover connectome of mammalian bipolar cells. *J. Comp. Neurol.* 527, 87–116. <https://doi.org/10.1002/cne.24084>.
  42. Kolb, H. (1979). The inner plexiform layer in the retina of the cat: electron microscopic observations. *J. Neurocytol.* 8, 295–329. <https://doi.org/10.1007/BF01236124>.
  43. McGuire, B.A., Stevens, J.K., and Sterling, P. (1984). Microcircuitry of bipolar cells in cat retina. *J. Neurosci.* 4, 2920–2938.
  44. Jacoby, R., Stafford, D., Kouyama, N., and Marshak, D. (1996). Synaptic inputs to ON parasol ganglion cells in the primate retina. *J. Neurosci.* 16, 8041–8056.
  45. Jacoby, R.A., and Marshak, D.W. (2000). Synaptic connections of DB3 diffuse bipolar cell axons in macaque retina. *J. Comp. Neurol.* 416, 19–29. [https://doi.org/10.1002/\(sici\)1096-9861\(2000103\)416:1<19::aid-cne3>3.0.co;2-h](https://doi.org/10.1002/(sici)1096-9861(2000103)416:1<19::aid-cne3>3.0.co;2-h).
  46. Jusuf, P.R., Lee, S.C.S., and Grünert, U. (2004). Synaptic connectivity of the diffuse bipolar cell type DB6 in the inner plexiform layer of primate retina. *J. Comp. Neurol.* 469, 494–506. <https://doi.org/10.1002/cne.11027>.
  47. Ding, H., Smith, R.G., Poleg-Polsky, A., Diamond, J.S., and Briggman, K.L. (2016). Species-specific wiring for direction selectivity in the mammalian retina. *Nature* 535, 105–110. <https://doi.org/10.1038/nature18609>.
  48. Stabio, M.E., Sabbah, S., Quattrochi, L.E., Ilardi, M.C., Fogerson, P.M., Leyrer, M.L., Kim, M.T., Kim, I., Schiel, M., Renna, J.M., et al. (2018). The M5 cell: a color-opponent intrinsically photosensitive retinal ganglion cell. *Neuron* 97, 251. <https://doi.org/10.1016/j.neuron.2017.12.030>.
  49. Sabbah, S., Papendorp, C., Behrendt, I., Rasras, H., Cann, J., Leyrer, M.L., Koplas, E., Beltoja, M., Etebari, C., Gunesch, A.N., et al. (2022). Intrinsically photosensitive retinal ganglion cells evade temporal filtering to encode environmental light intensity. Preprint at bioRxiv. <https://doi.org/10.1101/2022.04.09.487733>.
  50. Famiglietti, E.V. (1992). Polyaxonal amacrine cells of rabbit retina: PA2, PA3, and PA4 cells. Light and electron microscopic studies with a functional interpretation. *J. Comp. Neurol.* 316, 422–446. <https://doi.org/10.1002/cne.903160404>.
  51. Völgyi, B., Xin, D., Amarillo, Y., and Bloomfield, S.A. (2001). Morphology and physiology of the polyaxonal amacrine cells in the rabbit retina. *J. Comp. Neurol.* 440, 109–125. <https://doi.org/10.1002/cne.1373>.
  52. Davenport, C.M., Detwiler, P.B., and Dacey, D.M. (2007). Functional polarity of dendrites and axons of primate A1 amacrine cells. *Vis. Neurosci.* 24, 449–457. <https://doi.org/10.1017/S0952523807070010>.
  53. Sinha, R., Siddiqui, T.J., Padmanabhan, N., Wallin, J., Zhang, C., Karimi, B., Rieke, F., Craig, A.M., Wong, R.O., and Hoon, M. (2020). LRRTM4: a novel regulator of presynaptic inhibition and ribbon synapse arrangements of retinal bipolar cells. *Neuron* 105, 1007–1017.e5. <https://doi.org/10.1016/j.neuron.2019.12.028>.
  54. Foss, R.Y., and Miyamasu, W. (1973). Synaptic analysis of inner plexiform layer in human retina. *J. Comp. Neurol.* 147, 447–454. <https://doi.org/10.1002/cne.901470403>.
  55. Kerschensteiner, D., Morgan, J.L., Parker, E.D., Lewis, R.M., and Wong, R.O.L. (2009). Neurotransmission selectively regulates synapse formation in parallel circuits in vivo. *Nature* 460, 1016–1020. <https://doi.org/10.1038/nature08236>.
  56. Schiavo, G., Benfenati, F., Poulain, B., Rossetto, O., Poverino de Laureto, P., DasGupta, B.R., and Montecucco, C. (1992). Tetanus and botulinum-B neurotoxins block neurotransmitter release by proteolytic cleavage of synaptobrevin. *Nature* 359, 832–835. <https://doi.org/10.1038/359832a0>.
  57. Kim, H.L., Jeon, J.H., Koo, T.H., Lee, U.Y., Jeong, E., Chun, M.H., Moon, J.I., Massey, S.C., and Kim, I.B. (2012). Axonal synapses utilize multiple synaptic ribbons in the mammalian retina. *PLoS One* 7, e52295. <https://doi.org/10.1371/journal.pone.0052295>.
  58. Famiglietti, E.V. (1991). Synaptic organization of starburst amacrine cells in rabbit retina: analysis of serial thin sections by electron microscopy and graphic reconstruction. *J. Comp. Neurol.* 309, 40–70. <https://doi.org/10.1002/cne.903090105>.
  59. Midorikawa, M., Tsukamoto, Y., Berglund, K., Ishii, M., and Tachibana, M. (2007). Different roles of ribbon-associated and ribbon-free active zones in retinal bipolar cells. *Nat. Neurosci.* 10, 1268–1276. <https://doi.org/10.1038/nn1963>.
  60. Bloss, E.B., Cembrowski, M.S., Karsh, B., Colonnell, J., Fetter, R.D., and Spruston, N. (2018). Single excitatory axons form clustered synapses onto CA1 pyramidal cell dendrites. *Nat. Neurosci.* 21, 353–363. <https://doi.org/10.1038/s41593-018-0084-6>.
  61. Brun, V.H., Otnass, M.K., Molden, S., Steffenach, H.A., Witter, M.P., Moser, M.B., and Moser, E.I. (2002). Place cells and place recognition maintained by direct entorhinal-hippocampal circuitry. *Science* 296, 2243–2246. <https://doi.org/10.1126/science.1071089>.
  62. Hargreaves, E.L., Rao, G., Lee, I., and Knierim, J.J. (2005). Major dissociation between medial and lateral entorhinal input to dorsal hippocampus. *Science* 308, 1792–1794. <https://doi.org/10.1126/science.1110449>.
  63. Ito, H.T., Zhang, S.J., Witter, M.P., Moser, E.I., and Moser, M.B. (2015). A prefrontal-thalamo-hippocampal circuit for goal-directed spatial navigation. *Nature* 522, 50–55. <https://doi.org/10.1038/nature14396>.



64. Lagnado, L., and Schmitz, F. (2015). Ribbon synapses and visual processing in the retina. *Annu. Rev. Vis. Sci.* 7, 235–262. <https://doi.org/10.1146/annurev-vision-082114-035709>.
65. Zenisek, D. (2008). Vesicle association and exocytosis at ribbon and extra-ribbon sites in retinal bipolar cell presynaptic terminals. *Proc. Natl. Acad. Sci. USA* 105, 4922–4927. <https://doi.org/10.1073/pnas.0709067105>.
66. Chen, M., Van Hook, M.J., Zenisek, D., and Thoreson, W.B. (2013). Properties of ribbon and non-ribbon release from rod photoreceptors revealed by visualizing individual synaptic vesicles. *J. Neurosci.* 33, 2071–2086. <https://doi.org/10.1523/JNEUROSCI.3426-12.2013>.
67. Mehta, B., Ke, J.B., Zhang, L., Baden, A.D., Markowitz, A.L., Nayak, S., Briggman, K.L., Zenisek, D., and Singer, J.H. (2014). Global Ca<sup>2+</sup> signaling drives ribbon-independent synaptic transmission at rod bipolar cell synapses. *J. Neurosci.* 34, 6233–6244. <https://doi.org/10.1523/JNEUROSCI.5324-13.2014>.
68. Do, M.T.H. (2019). Melanopsin and the intrinsically photosensitive retinal ganglion cells: biophysics to behavior. *Neuron* 104, 205–226. <https://doi.org/10.1016/j.neuron.2019.07.016>.
69. Aranda, M.L., and Schmidt, T.M. (2021). Diversity of intrinsically photosensitive retinal ganglion cells: circuits and functions. *Cell. Mol. Life Sci.* 78, 889–907. <https://doi.org/10.1007/s00018-020-03641-5>.
70. Yu, W.Q., El-Danaf, R.N., Okawa, H., Pacholec, J.M., Matti, U., Schwarz, K., Odermatt, B., Dunn, F.A., Lagnado, L., Schmitz, F., et al. (2018). Synaptic convergence patterns onto retinal ganglion cells are preserved despite topographic variation in pre- and postsynaptic territories. *Cell Rep.* 25, 2017–2026.e3. <https://doi.org/10.1016/j.celrep.2018.10.089>.
71. Okawa, H., Yu, W.Q., Matti, U., Schwarz, K., Odermatt, B., Zhong, H., Tsukamoto, Y., Lagnado, L., Rieke, F., Schmitz, F., and Wong, R.O.L. (2019). Dynamic assembly of ribbon synapses and circuit maintenance in a vertebrate sensory system. *Nat. Commun.* 10, 2167. <https://doi.org/10.1038/s41467-019-10123-1>.
72. Anderson, J.R., Jones, B.W., Yang, J.H., Shaw, M.V., Watt, C.B., Koshevoy, P., Spaltenstein, J., Jurrus, E., U V, K., Whitaker, R.T., et al. (2009). A computational framework for ultrastructural mapping of neural circuitry. *PLoS Biol.* 7, e1000074. <https://doi.org/10.1371/journal.pbio.1000074>.
73. Anderson, J.R., Mohammed, S., Grimm, B., Jones, B.W., Koshevoy, P., Tasdizen, T., Whitaker, R., and Marc, R.E. (2011). The Viking viewer for connectomics: scalable multi-user annotation and summarization of large volume data sets. *J. Microsc.* 241, 13–28. <https://doi.org/10.1111/j.1365-2818.2010.03402.x>.
74. Della Santina, L., Kuo, S.P., Yoshimatsu, T., Okawa, H., Suzuki, S.C., Hoon, M., Tsuboyama, K., Rieke, F., and Wong, R.O.L. (2016). Glutamatergic monopolar interneurons provide a novel pathway of excitation in the mouse retina. *Curr. Biol.* 26, 2070–2077. <https://doi.org/10.1016/j.cub.2016.06.016>.
75. Cardona, A., Saalfeld, S., Schindelin, J., Arganda-Carreras, I., Preibisch, S., Longair, M., Tomancak, P., Hartenstein, V., and Douglas, R.J. (2012). TrakEM2 software for neural circuit reconstruction. *PLoS One* 7, e38011. <https://doi.org/10.1371/journal.pone.0038011>.
76. Boergens, K.M., Berning, M., Bocklisch, T., Bräunlein, D., Drawitsch, F., Frohnhofen, J., Herold, T., Otto, P., Rzepka, N., Werkmeister, T., et al. (2017). webKnossos: efficient online 3D data annotation for connectomics. *Nat. Methods* 14, 691–694. <https://doi.org/10.1038/nmeth.4331>.
77. Dowling, J.E., and Boycott, B.B. (1966). Organization of the primate retina: electron microscopy. *Proc. R. Soc. Lond. B Biol. Sci.* 166, 80–111.
78. Behrens, C., Schubert, T., Haverkamp, S., Euler, T., and Berens, P. (2016). Connectivity map of bipolar cells and photoreceptors in the mouse retina. *Elife* 5, e20041. <https://doi.org/10.7554/eLife.20041>.
79. Marc, R.E., Jones, B.W., Watt, C.B., Anderson, J.R., Sigulinsky, C., and Lauritzen, S. (2013). Retinal connectomics: towards complete, accurate networks. *Prog. Retin. Eye Res.* 37, 141–162. <https://doi.org/10.1016/j.preteyeres.2013.08.002>.
80. Marc, R.E., Anderson, J.R., Jones, B.W., Sigulinsky, C.L., and Lauritzen, J.S. (2014). The All amacrine cell connectome: a dense network hub. *Front. Neural Circ.* 8, 104. <https://doi.org/10.3389/fncir.2014.00104>.
81. Pfeiffer, R.L., Anderson, J.R., Dahal, J., Garcia, J.C., Yang, J.H., Sigulinsky, C.L., Rapp, K., Emrich, D.P., Watt, C.B., Johnston, H.A., et al. (2020). A pathoconnectome of early neurodegeneration: network changes in retinal degeneration. *Exp. Eye Res.* 199, 108196. <https://doi.org/10.1016/j.exer.2020.108196>.



## STAR★METHODS

### KEY RESOURCES TABLE

| REAGENT or RESOURCE                    | SOURCE                     | IDENTIFIER  |
|--|----------------------------|---|
| Experimental models: Organisms/strains |                            |   |
| Mouse model: <i>Gjd2-GFP</i>           | MMRRC                      | <i>Tg(Gjd2-EGFP)JM16Gsat/Mmucd</i> ;<br>RRID:MMRRC_030611-UCD   |
| Deposited data                         |                            |   |
| Retinal Connectome 1 (RC1)             | Marc/Jones Lab, Utah       | <a href="https://connectomes.utah.edu">https://connectomes.utah.edu</a>   |
| Mouse SBFSEM dataset                   | Kevin Briggman             | k0725 <a href="https://webknossos.org/publications/5c98dfbcbe67ded57f0c9061">https://webknossos.org/publications/5c98dfbcbe67ded57f0c9061</a> |
| Software and algorithms                |                            |   |
| ImageJ                                 | NIH                        | <a href="https://imagej.nih.gov/ij/">https://imagej.nih.gov/ij/</a> ;<br>RRID: SCR_003070   |
| Amira                                  | Thermo-Fisher Scientific   | <a href="https://www.feri.com/software/amira-avizo/">https://www.feri.com/software/amira-avizo/</a> ;<br>RRID: SCR_014305                     |
| Python v3.8.5                          | Python software foundation | <a href="http://www.python.org/">http://www.python.org/</a> ;<br>RRID:SCR_008394  |
| webKnossos                             | Open Source                | <a href="https://webknossos.org/">https://webknossos.org/</a> ;<br>RRID:SCR_020979  |
| Viking Viewer for Connectomics         | Marc/Jones Lab, Utah       | RRID: SCR_005986  |
| VikingPlot                             | Marc/Jones Lab, Utah       | <a href="https://zenodo.org/record/3234870#.XO7Y7lhKguU">https://zenodo.org/record/3234870#.XO7Y7lhKguU</a>                                   |

### RESOURCE AVAILABILITY

#### Lead contact

Further information and requests for resources and reagents should be directed to and will be fulfilled by the lead contact, Rachel O. Wong ([wongr2@uw.edu](mailto:wongr2@uw.edu)).

#### Materials availability

This study did not generate new, unique reagents.

#### Data and code availability

- The RC1 dataset is available once installing Viking (free) at <http://connectomes.utah.edu>. The volume URL is: <http://connectomes.utah.edu/Rabbit/volume.vikingxml>. Export of Viking data for these and other programs (e.g., Microsoft Excel) is available here: <https://connectomes.utah.edu/export/toctree.html>. The mouse volume k0725 from Ding et al.<sup>47</sup> is available at <https://webknossos.org/publications/5c98dfbcbe67ded57f0c9061>. The mouse volume generated in this study will be shared by the lead contact upon request.
- The custom, open-source software tools for annotation, viewing, and rendering are freely available: Viking (RRID:SCR\_005986)<sup>72</sup> and VikingPlot (<https://zenodo.org/record/3234870#.XO7Y7lhKguU>).<sup>39,73</sup>
- Any additional information required to reanalyze the data reported in this paper is available from the lead contact upon request.

### EXPERIMENTAL MODEL AND SUBJECT DETAILS

All procedures were conducted in accordance with University of Washington Institutional Animal Care and Use Committee guidelines, Institutional Animal Care and Use protocols of the University of Utah, the ARVO Statement for the Use of Animals in Ophthalmic and Visual Research, and the Policies on the Use of Animals and Humans in Neuroscience Research of the Society for Neuroscience. A young adult (2 month old) GJD2-GFP mouse (Tg (Gjd2-EGFP)JM16Gsat) was used in this study.



## METHOD DETAILS

### Tissue preparation and serial-block face electron microscopy

Mice were cervically dislocated and the eyes were enucleated. The retinas were dissected from eyecups in Ames' solution (Sigma) bubbled with 95% O<sub>2</sub>/5% CO<sub>2</sub>. Retinal pieces were fixed with 4% glutaraldehyde in 0.1M sodium cacodylate buffer, pH 7.3–7.4 for 30 min to 1 h at room temperature. The samples were then prepared for the SBEM following the protocol below.<sup>74</sup> The tissue was washed 3 times (5 min each time) in cold 0.1M cacodylate buffer and then incubated in reduced osmium made by combining equal parts 3% potassium ferrocyanide in 0.2M cacodylate buffer with 4% aqueous osmium tetroxide for 1 h in the fridge. After washing in double-distilled H<sub>2</sub>O (ddH<sub>2</sub>O), the tissue was placed in a freshly made thiocarbohydrazide solution (0.1g TCH in 10 mL dd H<sub>2</sub>O and placed in a 60°C oven for 1 h) for 20 min at room temperature (RT). After another rinse in ddH<sub>2</sub>O, the tissue was incubated in 2% osmium tetroxide (aqueous) for 30 min at RT. The samples were rinsed again and incubated in 1% uranyl acetate at 4°C overnight, washed and stained with Walton's lead aspartate for 30 min at 60°C. After another wash, the retinal piece was dehydrated with graded alcohol series: 20%, 50%, 70%, 90%, 100%, 100% ethanol, 5 min each, followed by 2 changes of 100% propylene oxide at RT for 10 min. Finally, the tissue was embedded in Epon. The block was then trimmed and mounted in the SBEM microscope (GATAN/Zeiss SIGMA, 3View). Image stacks were acquired at a voxel size of 5 × 5 × 50 nm.

### Volume reconstruction and image analysis

EM micrographs were aligned and registered using a customized program by AIVIA. Stitched and aligned images were loaded in ImageJ/TrakEM2<sup>75</sup> or webKnossos.<sup>76</sup> Analysis of OFF CBC output synapses was performed using webKnossos. OFF CBCs and their postsynaptic partners were traced as skeletons. An example cell of each OFF CBC type and their synapses were manually segmented. Analysis of ON CBC output synapses was performed using TrakEM2. The somata and processes of neurons were manually traced and segmented using TrakEM2 TreeLine and AreaTree functions. Synapses were annotated using the AreaList function, and vesicles were annotated using the ball function of TrakEM2. Bipolar cells, amacrine cells, and retinal ganglion cells were identified based on criteria described in previous literature.<sup>24,42,77</sup> Axonal processes of bipolar cells contain synaptic vesicles and ribbons. Generally, processes containing synaptic vesicles without ribbons (conventional synapses) are formed by amacrine cells. 3D reconstruction of the processes enabled us to further distinguish bipolar cells containing ribbonless synapses from amacrine cells. Dendrites of retinal ganglion cells are postsynaptic to bipolar and amacrine cells. They lack synaptic vesicles but contain microtubules. Whenever possible, processes were traced to the somata and axons to confirm the identity of retinal ganglion cells. Types of bipolar cells were determined based on their axonal stratification depth and arbor size.<sup>17,32,78</sup>

The 3D objects of either the skeletons of traced cells or the 3D volume segmentations were visualized and exported using 3D Viewer in TrakEM2. Final visualization of each 3D reconstruction was rendered in Amira (Thermo Fisher Scientific). An additional SBEM volume acquired previously by Ding et al.<sup>47</sup> was used to identify synaptic arrangements between T9 bipolar cells and their postsynaptic retinal ganglion cells, using the webKnossos online platform for 3D image visualization and annotation.<sup>76</sup>

Analysis of rabbit CBC output synapses was based on Retinal Connectome 1 (RC1), a high-resolution (2.18 nm/pixel) connectomics dataset generated from an adult (13 month old) female Dutch Belted rabbit retina using transmission electron microscopy (TEM). The tissue collection and processing, TEM imaging, and the construction, viewing, and annotation of the volume are extensively detailed.<sup>33,39,40,72,73,79,80</sup>

Identification and subsequent classification of the rabbit ON CBCs analyzed in this study are detailed in Sigulinsky et al.<sup>33</sup> The output synapses of 3 cells for each of the seven rabbit ON CBC classes (except CbBwf) were reexamined to identify multiribbon synapses, refine the criteria for ribbonless synapses, and segregate into axon versus terminal localization. Both CbBwf cells are incomplete due to their large size and extension beyond the volume boundaries. Ribbonless synapses in previous reports from RC1 termed these structures "bipolar conventional synapses", abbreviated as "BCS".<sup>33,39–41,72,73,79–81</sup> Ribbonless synapses in the RC1 dataset present as a thin, electron dense membrane on the presynaptic side with at least one tethered or merged synaptic vesicle, a thick and splotchy electron dense membrane on the postsynaptic cell (with or without associated cytoplasmic electron densities), and a widening and presence of tethers within the extracellular space between the partner cells compared to surrounding regions. In short, these ribbonless synapses exhibit all of the same features as canonical ribbon synapses, but lack the characteristic lamella and halo of tethered synaptic vesicles of the presynaptic ribbon specialization, as well as the cytoplasmic arciform density of the ribbon-anchoring assembly. Scaling of the rabbit TEM data differs from the mouse SEM data for the purpose of displaying the features underlying the criteria for synapse identification. Cell reconstructions were created from the Viking annotations and rendered using VikingPlot.

## QUANTIFICATION AND STATISTICAL ANALYSIS

Statistical analysis was performed using Python 3.8.5. Two-sided Wilcoxon Rank-Sum test was used to compare two groups of samples. Kruskal-Wallis H-test was used to compare more than two groups of data. Post-hoc Wilcoxon test was performed subsequently. Chi-square test was performed on the raw counting numbers when examining whether observed frequencies matched the expected ones or whether the observed frequencies across different sample groups are the same. Significance was determined at  $p < 0.05$ .

Cell Reports, Volume 42

**Supplemental information**

**Distinctive synaptic structural motifs  
link excitatory retinal interneurons  
to diverse postsynaptic partner types**

**Wan-Qing Yu, Rachael Swanstrom, Crystal L. Sigulinsky, Richard M. Ahlquist, Sharm  
Knecht, Bryan W. Jones, David M. Berson, and Rachel O. Wong**

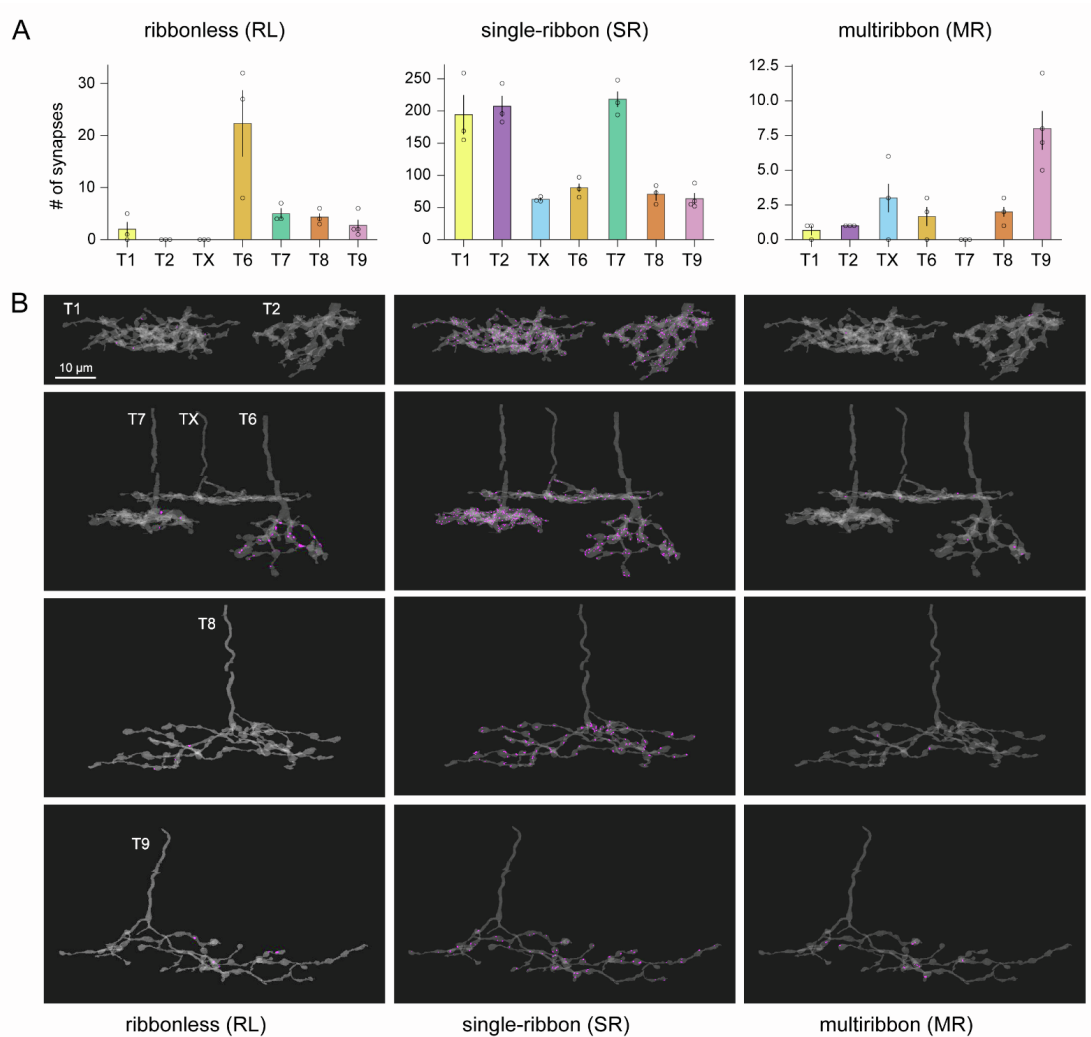


**Figure S1. The number and spatial distribution of three distinct presynaptic arrangements, Related to Figure 1.** The number (A) and spatial distribution (B) of ribbonless (RL), single-ribbon (SR) and multiribbon (MR) synapses on the axonal terminal arbors of example CBCs of each type analyzed in the mouse retina. Each data point represents a CBC. Error bars, S.E.M.

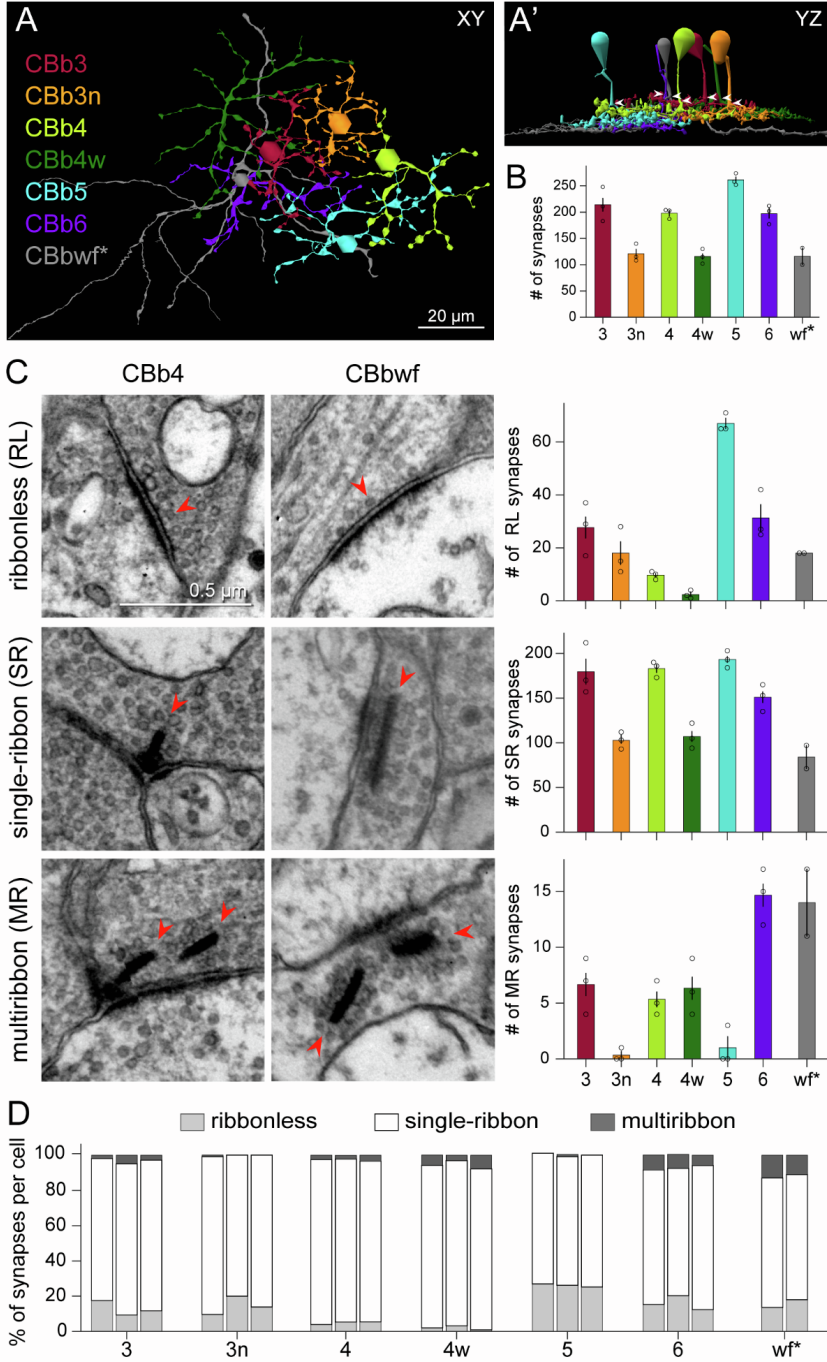
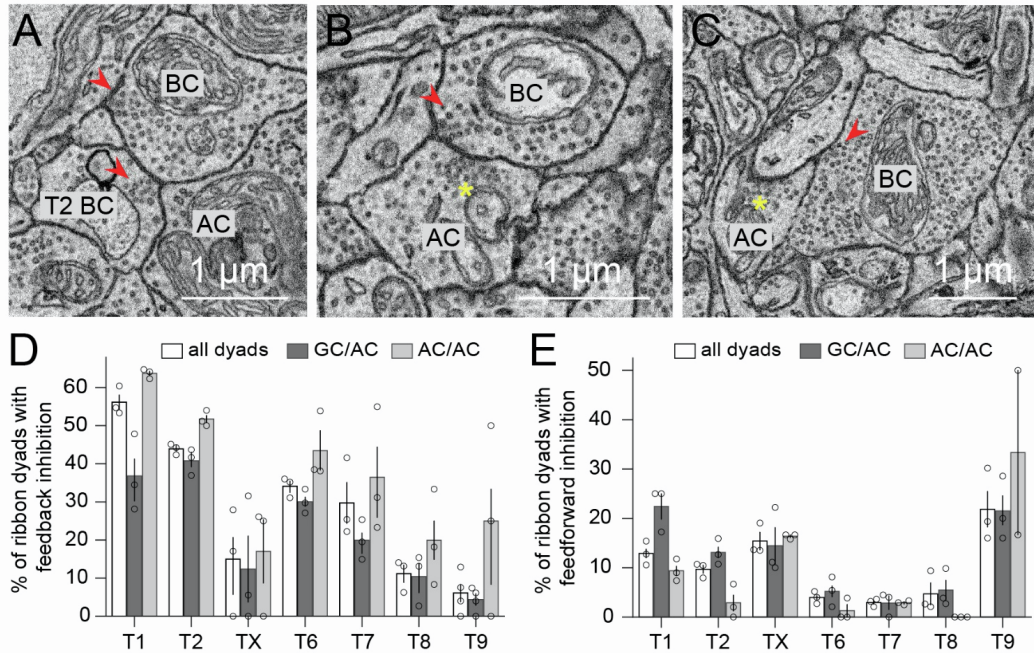
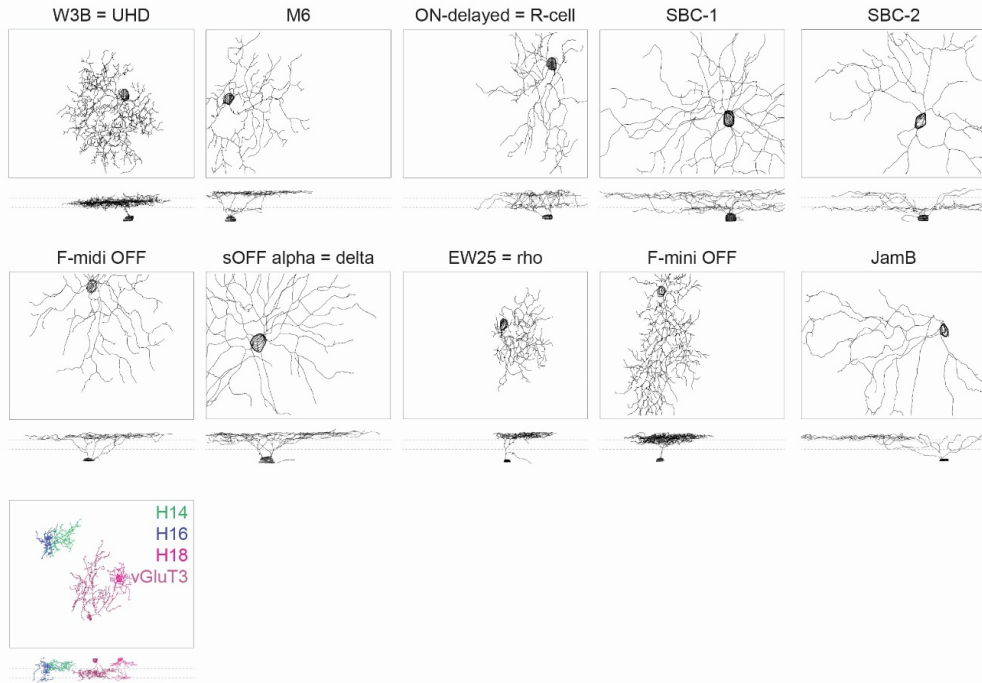


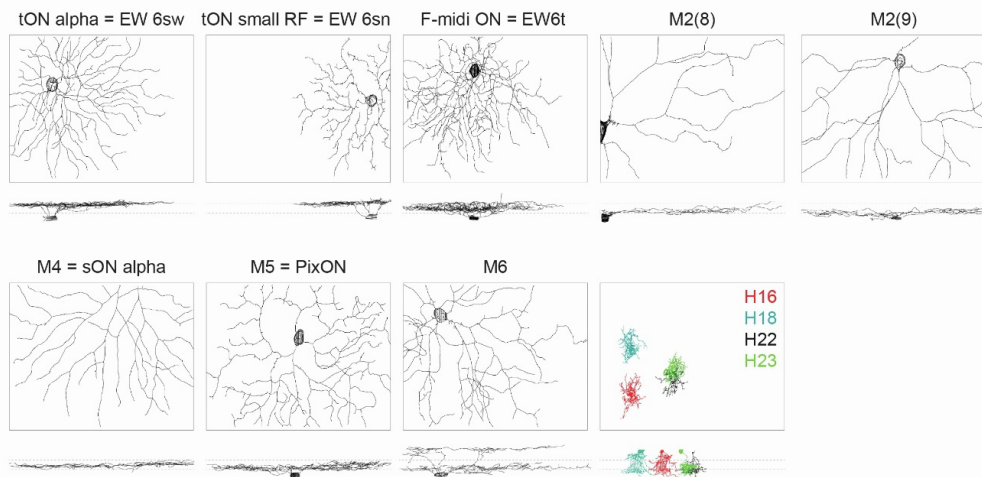
**Figure S2. Rabbit ON CBCs exhibit three distinct presynaptic arrangements, Related to Figure 1.** (A, A') Rendered reconstructions of the axonal terminals for representative examples of the seven ON CBC types (CBb3, CBb3n, CBb4, CBb4w, CBb5, CBb6, CBbwf) created from serial TEM sections. En face (A) and side (A') views. Note that the side profile (A') is a 90° rotation of the en face view in A. \*CBbwf axonal arbor reconstructions are incomplete due to their large size exceeding the EM volume. (B) Total number of output synapses on each axonal arbor of the seven classes/types of ON CBCs. All output synapses on the arbor beyond the branching point shown by the arrowheads were mapped. (C) Representative examples of ribbonless (RL), single-ribbon (SR) and multiribbon (MR) output synapse arrangements formed by CBb4 (left column) and CBbwf (middle column) CBCs. Arrowheads indicate presynaptic vesicles at the synaptic contact (RL) or synaptic ribbons (SR, MR). Structure lookup numbers for CBb4 examples in RC1 dataset: RL = 125159, SR = 167887, MR = 46702 & 46703; for CBbwf examples: RL = 16147, SR = 28114, MR = 119804 & 119805. (D) The percentage of each presynapse arrangement per cell formed by the seven classes/types of ON CBCs (right column). Each data point represents a CBC. Error bars = S.E.M. Abbreviations: 3, CBb3; 3n, CBb3n; 4, CBb4; 4w, CBb4w; 5, CBb5; 6, CBb6; wf, CBbwf.



Postsynaptic Partner Types of T2 BC



Postsynaptic Partner Types of T6 BC



100  $\mu$ m

**Figure S4. A gallery showing an example of the ganglion cell (GC) and narrow-field amacrine cell (AC) types synaptically connected to T2 and T6 cone bipolar cells (CBCs), Related to Figure 4.** We identified 14 (10 RGC and 4 narrow-field AC types) and 12 (8 RGC and 4 narrow-field AC types) cell types that received ribbon input from T2 and T6 CBCs, respectively. T2 and T6 CBCs also synapse onto wide-field ACs, but due to their large arbors that extended beyond the volume, we could not confidently identify their cell type.

**Table S1. Total number of synapses, number of synapses identified for each synaptic motif, and counts of each synaptic motif with different postsynaptic compositions for each CBC examined in the mouse retina, Related to Figures 2 – 3.**

| BC type | BC ID | total # | ribbonless |     |      | single ribbon synapses |     |      |      |      |       |       |       | multiribbon synapses |        |
|---------|-------|---------|------------|-----|------|------------------------|-----|------|------|------|-------|-------|-------|----------------------|--------|
|         |       |         | monad      |     |      | monad                  |     |      | dyad |      |       | triad | monad | dyad                 |        |
|         |       |         | #          | 1AC | 1RGC | #                      | 1AC | 1RGC | #    | 2ACs | 2RGCs |       |       |                      | RGC/AC |
| T1      | BC1   | 265     | 5          | 1   | 3    | 14                     | 10  | 4    | 182  | 123  | 0     | 59    | 51    | 0                    | 1      |
|         | BC2   | 156     | 1          | 0   | 1    | 7                      | 5   | 2    | 102  | 78   | 0     | 24    | 30    | 0                    | 0      |
|         | BC3   | 170     | 0          | 0   | 0    | 8                      | 8   | 0    | 117  | 85   | 0     | 32    | 26    | 0                    | 1      |
| T2      | BC1   | 197     | 0          | 0   | 0    | 4                      | 1   | 3    | 142  | 43   | 8     | 88    | 6     | 0                    | 1      |
|         | BC2   | 244     | 0          | 0   | 0    | 7                      | 5   | 2    | 182  | 50   | 15    | 115   | 13    | 0                    | 0      |
|         | BC3   | 184     | 0          | 0   | 0    | 8                      | 3   | 5    | 121  | 30   | 17    | 72    | 16    | 1                    | 0      |
| TX      | BC1   | 64      | 0          | 0   | 0    | 16                     | 16  | 0    | 37   | 19   | 0     | 18    | 0     | 2                    | 1      |
|         | BC2   | 60      | 0          | 0   | 0    | 14                     | 13  | 1    | 44   | 24   | 0     | 20    | 0     | 0                    | 0      |
|         | BC3   | 73      | 0          | 0   | 0    | 19                     | 15  | 4    | 42   | 24   | 0     | 18    | 0     | 1                    | 5      |
| T6      | BC1   | 109     | 27         | 26  | 1    | 12                     | 9   | 3    | 58   | 21   | 0     | 37    | 0     | 0                    | 3      |
|         | BC2   | 74      | 8          | 6   | 0    | 5                      | 4   | 1    | 55   | 13   | 5     | 37    | 0     | 0                    | 0      |
|         | BC3   | 131     | 26         | 24  | 2    | 12                     | 12  | 0    | 77   | 26   | 3     | 48    | 0     | 0                    | 2      |
| T7      | BC1   | 198     | 3          | 3   | 0    | 3                      | 3   | 0    | 168  | 91   | 2     | 75    | 0     | 0                    | 0      |
|         | BC2   | 255     | 4          | 4   | 0    | 16                     | 14  | 2    | 190  | 122  | 1     | 67    | 11    | 0                    | 0      |
|         | BC3   | 217     | 4          | 3   | 1    | 14                     | 13  | 1    | 145  | 103  | 1     | 41    | 8     | 0                    | 0      |
| T8      | BC1   | 89      | 3          | 3   | 0    | 15                     | 9   | 5    | 66   | 3    | 2     | 61    | 0     | 1                    | 1      |
|         | BC2   | 80      | 4          | 3   | 1    | 15                     | 10  | 5    | 53   | 11   | 5     | 37    | 0     | 2                    | 1      |
|         | BC3   | 62      | 6          | 6   | 0    | 9                      | 7   | 2    | 41   | 12   | 3     | 26    | 0     | 0                    | 1      |
| T9      | BC1   | 69      | 6          | 1   | 5    | 16                     | 3   | 13   | 31   | 4    | 0     | 27    | 0     | 3                    | 5      |
|         | BC2   | 66      | 1          | 1   | 0    | 20                     | 9   | 11   | 32   | 6    | 1     | 25    | 0     | 1                    | 4      |
|         | BC3   | 102     | 2          | 0   | 2    | 24                     | 10  | 14   | 53   | 4    | 0     | 49    | 0     | 10                   | 2      |
|         | BC4   | 61      | 2          | 1   | 1    | 15                     | 3   | 12   | 28   | 0    | 3     | 25    | 0     | 5                    | 2      |